Astronomy & Astrophysics manuscript no. February 22, 2006
(DOI: will be inserted by hand later)

Accurate photometric redshifts from the CFHT Legacy Survey calibrated on the VIMOS VLT Deep Survey

O. Ilbert[1,2], S. Arnouts[2], H.J. McCracken[3], M. Bolzonella[1], O. Le Fèvre[2], G. Zamorani[4], R. Pellò[5], A. Iovino[6], L. Tresse[2], D. Bottini[7], B. Garilli[7], V. Le Brun[2], D. Maccagni[7], Y. Mellier[3,8], J.P. Picat[5], R. Scaramella[9], M. Scodeggio[7], G. Vettolani[10], A. Zanichelli[10], C. Adami[1], S. Bardelli[4], E. Bertin[3], A. Cappi[4], S. Charlot[11,3], P. Ciliegi[4], T. Contini[5], O. Cucciati[6], S. Foucaud[7], P. Franzetti[7], I. Gavignaud[11], L. Guzzo[7], B. Marano[1], C. Marinoni[2,12], A. Mazure[2], B. Meneux[2], R. Merighi[4], S. Paltani[13,14], A. Pollo[2], L. Pozzetti[4], M. Radovich[15], E. Zucca[4], M. Bondi[10], A. Bongiorno[1], G. Busarello[15], S. De La Torre[2], L. Gregorini[6], F. Lamareille[5], G. Mathez[5], P. Merluzzi[15], V. Ripepi[15], D. Rizzo[5], and D. Vergani[7]

[1] Università di Bologna, Dipartimento di Astronomia - Via Ranzani 1, 40127, Bologna, Italy
[2] Laboratoire d'Astrophysique de Marseille, UMR 6110 CNRS-Université de Provence, BP8, 13376 Marseille Cedex 12, France
[3] Institut d'Astrophysique de Paris, UMR 7095, 98 bis Bvd Arago, 75014 Paris, France
[4] INAF-Osservatorio Astronomico di Bologna - Via Ranzani 1, 40127, Bologna, Italy
[5] Laboratoire d'Astrophysique de l'Observatoire Midi-Pyrénées, UMR 5572, 14 avenue E. Belin, 31400 Toulouse, France
[6] INAF-Osservatorio Astronomico di Brera - Via Brera 28, Milan, Italy
[7] IASF-INAF - via Bassini 15, 20133, Milano, Italy
[8] Observatoire de Paris, LERMA, 61 Avenue de l'Observatoire, 75014 Paris, France
[9] INAF-Osservatorio Astronomico di Roma - Via di Frascati 33, 00040, Monte Porzio Catone, Italy
[10] IRA-INAF - Via Gobetti,101, 40129, Bologna, Italy
[11] European Southern Observatory, Garching, Germany
[12] Centre de Physique Théorique, Marseille, France
[13] Integral Science Data Centre, ch. d'Écogia 16, CH-1290 Versoix
[14] Geneva Observatory, ch. des Maillettes 51, CH-1290 Sauverny
[15] INAF-Osservatorio Astronomico di Capodimonte - Via Moiariello 16, 80131, Napoli, Italy

Received ... / Accepted ...

Abstract. We present and release photometric redshifts for an unprecedented large and deep sample of 522286 objects with $i'_{AB} \leq 25$ in the Canada-France Legacy Survey "Deep Survey" fields D1, D2, D3, and D4, over a field of 3.11 effective square degrees. We use 3241 spectroscopic redshifts with $0 \leq z \leq 5$ from the VIMOS VLT Deep Survey as a calibration and training set to derive photometric redshifts. Using the "Le Phare" photometric redshift code, we have devised a robust calibration method which removes systematic trends and greatly reduces by a factor of 2.3 the fraction of catastrophic errors, a significant improvement over methods classically used. Comparing spectroscopic and photometric redshifts, we assess in detail the accuracy and the robustness of the photometric redshift sample. For a sample selected at $i'_{AB} \leq 24$, we reach a redshift accuracy of $\sigma_{\Delta z/(1+z)} = 0.037$ with $\eta = 3.7\%$ of catastrophic errors (defined strictly as $\Delta z/(1+z) > 0.15$). As expected, the reliability of the photometric redshifts is lower for fainter objects: we find $\sigma_{\Delta z/(1+z)} = 0.029, 0.043$ and $\eta = 1.7\%, 5.4\%$ for samples selected at $i'_{AB} = 17.5 - 22.5, 22.5 - 24$ respectively. The photometric redshifts of starburst galaxies are the less reliable: the starburst galaxies represent 18% of the spectroscopic sample but 54% of the catastrophic errors. An analysis as a function of redshift demonstrates that our photometric redshifts function best in the redshift range $0.2 \leq z \leq 1.5$. We find an excellent agreement between the photometric and the VVDS spectroscopic redshift distributions at $i'_{AB} \leq 24$ on the CFHTLS-D1 field. Finally, we compare the redshift distributions of i' selected galaxies on the 4 CFHTLS deep fields, showing that cosmic variance is already present on fields of $0.7 - 0.9$ deg^2. These photometric redshifts are released to the French and Canadian communities at *http://* .

Key words. Galaxies: distances and redshifts - Galaxies: photometry - Methods: data analysis

1. Introduction

A key factor in the study of galaxy evolution is our ability to acquire large, deep, well-defined redshift samples on large volumes. Since the photometric redshift measurement relies only on the observed colors (Baum 1962), this method is an efficient way to assemble large and faint samples. The photometric redshift method is also the only way to estimate redshifts beyond the spectroscopic limit (Sawicki et al. 1997, Arnouts et al. 1999, Benítez 2000, Fontana et al. 2000, Bolzonella et al. 2002).

The price to pay for this efficiency is the accuracy and the robustness of the measurement. The most accurate photometric redshifts with medium band filters (Wolf et al. 2004) still remain 30 times less accurate than redshifts measured with low resolution spectroscopy (Le Fèvre et al. 2004b). For many statistical analysis, like the galaxy luminosity function, the velocity accuracy of photometric redshifts could be sufficient (Wolf et al. 2003). But the major limitation of the photometric redshift method remains the difficulty to detect and control systematic errors, mainly systematic offsets between spectroscopic and photometric redshifts, and 'catastrophic' failures with a difference between photometric and spectroscopic redshifts largely greater than the expected uncertainty.

At the first order, the photometric redshifts are reliable when the Balmer or Lyman continuum breaks can be observed between two broad band filters. Traditional sets of optical filters from the B to the I bands can measure redshifts between $0.2 < z < 1$. Near infrared data are required to provide robust photometric redshifts in the "redshift desert"at $z > 1.5$ since the Balmer break is redshifted to $\lambda > 10000$Å (Cimatti et al. 2002, Gabasch et al. 2004, Mobasher et al. 2004). At $z > 3$, reliable photometric redshifts may be estimated using deep U band data, based on the Lyman break visible at $\lambda > 3600$Å (e.g. Madau 1995).

The reliability of photometric redshifts is also related to the photometric redshift method. In the standard χ^2 method, the most likely redshift and type of each galaxy are determined by a template-fitting procedure, systematically fitting the observed photometry with a reference set of spectral templates (e.g. Puschell 1982). Since no spectroscopic information is a priori required, the standard χ^2 method can be extended beyond the spectroscopic limits (Bolzonella et al. 2002). As an alternative approach, the training methods extract the information from the spectroscopic sample to estimate the photometric redshifts, with for instance neural network methods (e.g. Vanzella et al. 2004) or empirical reconstruction of the redshift-color relation (e.g. Connolly et al. 1995, Wang et al. 1998, Csabai et al. 2000). However, if the redshift range is poorly represented in the training sample, these methods become uncertain. As an hybrid approach combining the advantages of these two methods, the standard χ^2 method can be tuned using a spectroscopic sample. For instance, the initial set of templates could be optimized (Budavári et al. 2000, Benítez 2004) or the spectroscopic redshift distribution could be introduced as an *a priori* knowledge in Bayesian methods (Benítez 2000). These last methods are using the spectroscopic information to improve the quality of the estimate and can also be extended beyond the spectroscopic limit.

One of the main limitation in obtaining accurate photometric redshifts to explore galaxy evolution is the quality and uniformity of the photometric magnitudes in large samples across large fields. We present here the photometric redshifts measured using the Canada-France Hawaii Telescope Legacy Survey "Deep Fields" catalogues (CFHTLS, *http://www.cfht.hawaii.edu/Science/CFHTLS*) processed at the TERAPIX data reduction centre[1] complemented with shallower VIMOS VLT Deep Survey multi-color data (McCracken et al. 2003, Le Fèvre et al. 2004a). We use the current release 'T03' of the CFHTLS. We focus on the deep field CFHTLS-D1 (or VVDS-0226-04) for which 11567 faint selected spectra $I_{AB} \leq 24.0$ are available from the VVDS spectroscopic survey (Le Fèvre et al. 2005a) and are used here as a training sample. We then compute photometric redshifts for all the CFHTLS "Deep Fields" D1, D2, D3, and D4 to obtain a large and deep dataset of 522286 objects at $i'_{AB} \leq 25$. Photometric and spectroscopic data are described in Section 2. Results obtained with the standard χ^2 method are presented in Section 3. We describe in Section 4 a method to calibrate the standard χ^2 method on spectroscopic data. The quality of these calibrated photometric redshifts is detailed in Section 5, as a function of redshift, apparent magnitude and spectral type. In Section 6, we investigate how the combination of different bands affects the accuracy of our photometric redshifts. We finally present in Section 7 the photometric redshifts with $i'_{AB} \leq 25$ in the 4 CFHTLS deep fields. The photometric redshift catalogs are released to the Canada-France community at *http://* . Analysis like the evolution of the angular correlation function or of the luminosity function will be presented in forthcoming papers.

Throughout the paper, we use a flat lambda cosmology ($\Omega_m = 0.3$, $\Omega_\Lambda = 0.7$) and we define $h = H_0/100$ km s^{-1} Mpc^{-1}. Magnitudes are given in the AB system. We use the notations zp for photometric redshift, zs for spectroscopic redshift and Δz for $zp - zs$.

2. Data description

CFHTLS multi-color data

The deep multi-color data from the Canada-France Hawaii Telescope Legacy Survey (CFHTLS) are imaged with the MegaCam CCD camera on the CFHT. This camera consists of 36 CCDs of 2048×4612 pixel and covers a field-of-view of 1 deg^2 with a resolution of 0.186 arcsec-

Send offprint requests to: O. Ilbert, e-mail: olivier.ilbert1@bo.astro.it

[1] terapix.iap.fr

ond per pixel. The multi-color data cover the observed wavelength range 3850Å $< \lambda <$ 8850Å in the u^*, g', r', i', z' filters (Fig.1). We analyse in this paper the deep fields CFHTLS-D1 (centered on $02^h25^m59^s - 04°29'40''$), CFHTLS-D2 ($10^h00^m28^s + 02°12'30''$), CFHTLS-D3 ($14^h19^m27^s + 52°40'56''$) and CFHTLS-D4 ($22^h15^m31^s - 17°43'56''$), focusing primarily on the CFHTLS-D1 field for which we have a large spectroscopic sample available from the VVDS. We use the release 'T03' of the CFHTLS. The data processing of the CFHTLS "deep fields" is described in McCracken et al. (2006, in preparation). Considerable attention has been devoted in the Terapix pipeline to produce highly accurate photometric zero-points to better than 0.05 mag, and accurate relative band to band astrometry allowing for precise color computation (McCracken et al. 2006, in preparation). Removing the masked area, the effective field-of-view is about 0.77, 0.69, 0.83 and 0.82 deg^2 for CFHTLS-D1, D2, D3 and D4 respectively. In CFHTLS-D1, the catalogue reaches the limiting magnitudes of $u^*_{AB} \sim 26.5$, $g'_{AB} \sim 26.4$, $r'_{AB} \sim 25.0$, $i'_{AB} \sim 25.9$ and $z'_{AB} \sim 25.0$ (corresponding to 50% completeness). The data in other CFHTLS "Deep Fields" are also extremely deep with a limiting magnitude $i'_{AB} \sim 25.7, 26.2, 26.0$ in the D2, D3, D4 respectively. A summary table listing the exposure times in each band is given on the Terapix web page (*http://terapix.iap.fr/*). Apparent magnitudes are measured using Kron-like elliptical aperture magnitudes (Kron 1980). The magnitudes are corrected from the galactic extinction estimated object by object from dust map images (Schlegel et al. 1998). We multiply all the SExtractor errors in the flux measurements (Bertin & Arnouts 1996) by a factor 1.5.

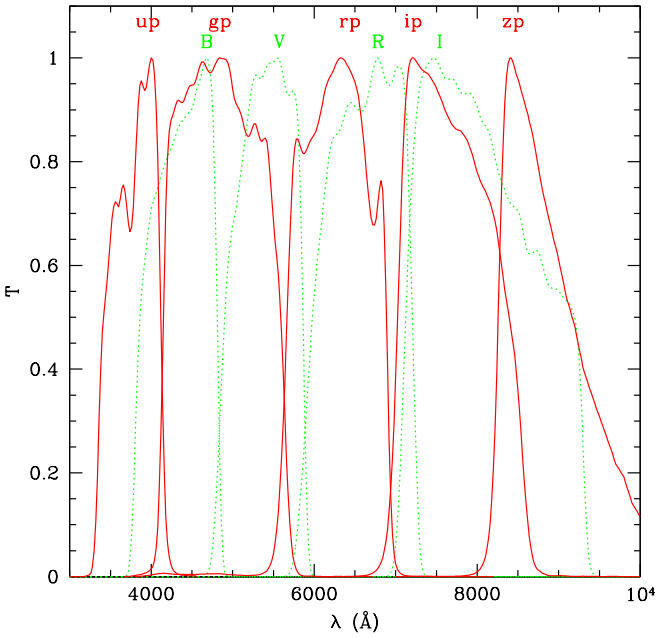

Fig. 1. CFHT transmissions curves normalized to unity. The solid lines correspond to the $u*$, g', r', i', z' filters used for the CFHTLS survey. The dotted lines correspond to the B, V, R, I filters used for the VVDS survey.

VVDS multi-color data

In addition to the CFHTLS data on the CFHTLS-D1 field, we use the shallower images from the VVDS survey acquired with the wide-field 12K mosaic camera on the CFHT (Le Fèvre et al. 2004a). McCracken et al. (2003) describe in detail the photometry and the astrometry of the VVDS-0226-04 field. The VVDS-0226-04 field covers the entire CFHTLS-D1 deep field and reaches the limiting magnitudes $B_{AB} \sim 26.5$, $V_{AB} \sim 26.2$, $R_{AB} \sim 25.9$ and $I_{AB} \sim 25.0$ (corresponding to 50% completeness). Near infrared data in J and Ks bands are also available over 160 arcmin^2 with the magnitude limits of $J_{AB} \sim 24.1$ and $K_{AB} \sim 23.8$ respectively (Iovino et al. 2005).

VVDS spectroscopic data

We use the VVDS spectroscopic data acquired with the multi-object spectrograph VIMOS installed at the ESO-VLT. In this paper, we consider the deep spectroscopic sample observed in the VVDS-0226-04 field (CFHTLS-D1) and selected according to the criterion $17.5 \leq I_{AB} \leq 24.0$ (Le Fèvre et al. 2005a). This sample consists in 11567 spectra. Four classes have been established to assess the quality of the spectroscopic redshift measurement, corresponding to a confidence level of 55%, 81%, 97% and 99% in the redshift measurement (Le Fèvre et al. 2005a). Since our goal is to assess the quality of the photometric redshifts including the fraction of catastrophic failures, we restrict ourselves to the classes with a confidence level greater or equal to 97%. In the sub-area in common with the CFHTLS-D1 field, the final spectroscopic sample used in this paper consists in 2867 galaxies, 364 stars and 31 QSOs, with highly reliable redshift measurements. The median redshift is about 0.76. The 1σ accuracy of the spectroscopic redshift measurements is estimated at 0.0009 from repeated VVDS observations.

To summarize, the multi-color data on the CFHTLS-D1 field consists in two joint $u*$, g', r', i', z' and B, V, R, I datasets over 0.77 deg^2, adding also J and K apparent magnitudes over 160 arcmin^2. For a given object, the photometric redshift is computed using all the available bands. These photometric redshifts are calibrated on 2867 spectroscopic redshifts with a confidence level greater or equal to 97%. As an illustration of our joined photometric and spectroscopic data set, Fig.2 shows the observed colors (only CFHTLS filters) as a function of the spectroscopic redshifts. The multi-color data available on the 3 other CFHTLS deep fields D2, D3, D4 are $u*$, g', r', i', z' apparent magnitudes.

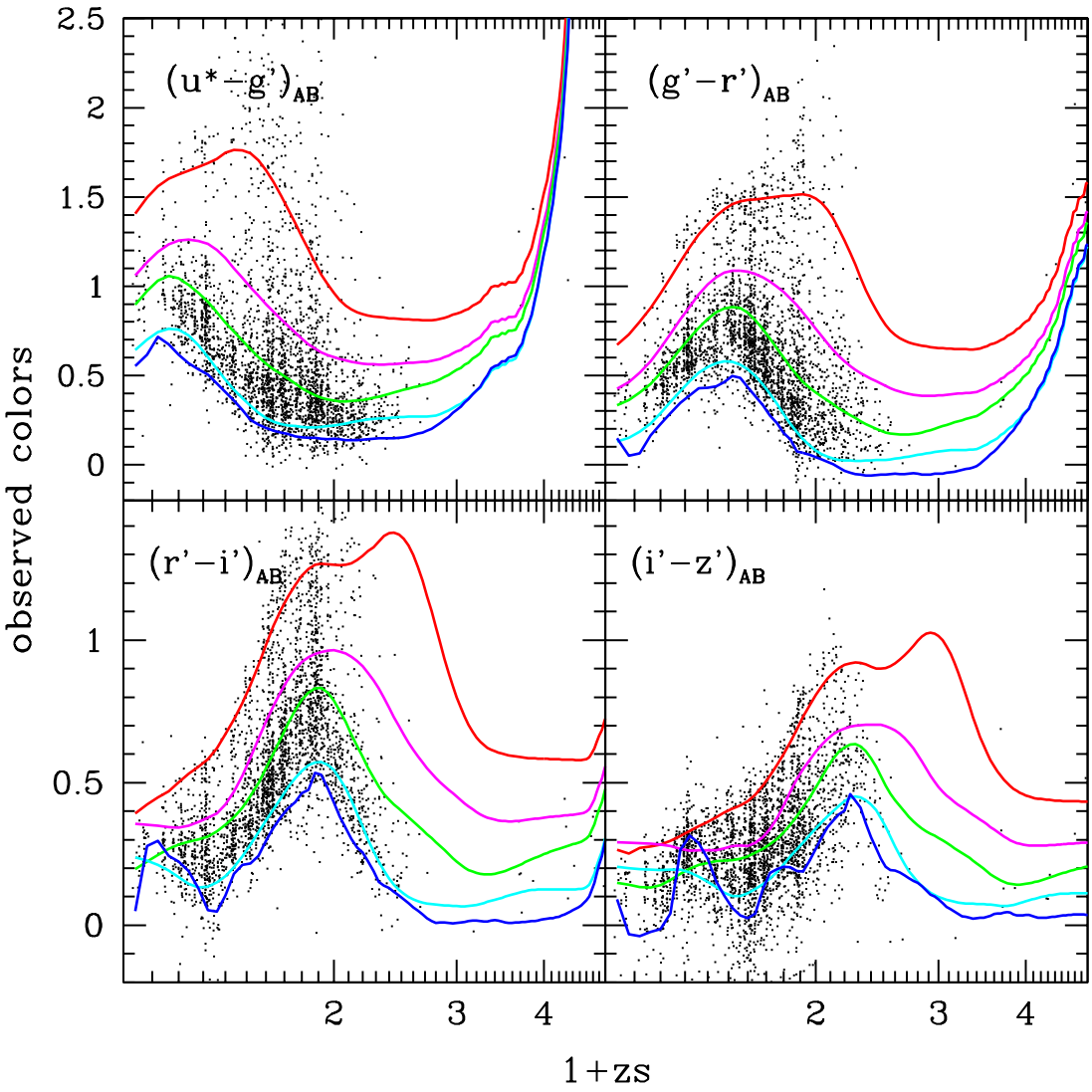

Fig. 2. Observed colors as a function of the spectroscopic redshifts (black points). The predicted colors derived from our optimized set of templates are shown with solid lines: Ell, Sbc, Scd, Irr (Coleman, Wu & Weedman 1980) and starburst (Kinney et al. 1996) from the top to the bottom, respectively.

3. Photometric redshifts with the standard χ^2 method

We present in this section the results obtained with a standard χ^2 method, without training the photometric redshift estimate on the spectroscopic sample.

3.1. The photometric redshift code *Le_Phare*

We apply the code *Le Phare*[2] (S. Arnouts & O. Ilbert) to compute the photometric redshifts. The standard χ^2 method is described in Arnouts et al. (1999, 2002). Results have been also cross-checked using the code Hyperz (Bolzonella et al. 2000).

The observed colors are matched with the colors predicted from a set of spectral energy distribution (SED). Each SED is redshifted in steps of $\Delta z = 0.04$ and convolved with the filter transmission curves (including instrument efficiency). The opacity of the inter-galactic medium (Madau 1995) is taken into account. The merit function χ^2 is defined as follow

$$\chi^2(z,T,A) = \sum_{f=1}^{N_f} \left(\frac{F^f_{\rm obs} - A \times F^f_{\rm pred}(z,T)}{\sigma^f_{\rm obs}} \right)^2, \qquad (1)$$

where $F^f_{\rm pred}(T,z)$ is the flux predicted for a template T at redshift z. $F^f_{\rm obs}$ is the observed flux and $\sigma^f_{\rm obs}$ the associated error. The index f refers to the considered filter and N_f is the number of filter. The photometric redshift is estimated from the minimization of χ^2 varying the three free parameters z, T and the normalization factor A.

[2] www.lam.oamp.fr/arnouts/LE_PHARE.html

3.2. Templates set

We use as our primary set of templates the four CWW observed spectra Ell, Sbc, Scd, Irr (Coleman, Wu & Weedman 1980) commonly used to estimate the photometric redshifts (Sawicki et al. 1997, Fernández-Soto et al. 1999, Arnouts et al. 1999, Brodwin et al. 2006). We add an observed starburst SED from Kinney et al. (1996) to improve the representativity of the CWW library. These templates are linearly extrapolated in the UV ($\lambda < 2000$Å) and extrapolated in the infrared with the GISSEL synthetic model (Bruzual et Charlot 2003). For spectral types later than Sbc, we allow a reddening $E(B-V) = 0, 0.05, 0.1, 0.15, 0.2$ following the interstellar extinction law measured in the Small Magellanic Cloud (Prevot et al. 1984). Even if these 5 templates are not fully representative of the variety of observed spectra, this reduces the possible degeneracies between predicted colors and redshift (Benítez 2000).

3.3. Results based on the standard χ^2 method

We apply the standard χ^2 method on the CFHTLS-D1 data. Fig.3 shows a comparison between the VVDS spectroscopic redshifts and the photometric redshifts at $i' \leq 22.5$. A clear systematic offset appears at $zs < 0.5$. Such a trend is not expected for a bright selected sample in a redshift range where the Balmer break is observed between the u^* and the r' band. Small uncertainties in the photometric zero-point calibration or an imperfect knowledge of the complete instrument transmission curve (filter+CCD+atmosphere+telescope) could explain such a systematic trend.

At fainter magnitude (top left panel of Fig.6, method *a)*), we observe a large fraction of galaxies with $\Delta z > 1$, mainly in the redshift range $1.5 < zp < 3$. Most of these catastrophic errors are caused by mis-identification of Lyman break and Balmer break. An illustration of this degeneracy is presented in Fig.4, showing the importance of NIR data to break this degeneracy. An alternative solution is to include a relevant information in the PDFz (redshift Probability Distribution Function) using the bayesian approach (e.g. Benítez 2000, Mobasher et al. 2004) in order to favor one of the two solutions, as is discussed in Section 4.3.

This basic comparison shows that blindly trusting photometric redshifts could be misleading. In the following, we will improve the photometric redshift quality using a training spectroscopic sample.

4. An improved method to compute robust photometric redshifts

As shown in section 3.3, spectroscopic redshifts are required to calibrate the standard χ^2 method. In this section, we describe the steps we have followed to calibrate the χ^2 photometric redshift estimate.

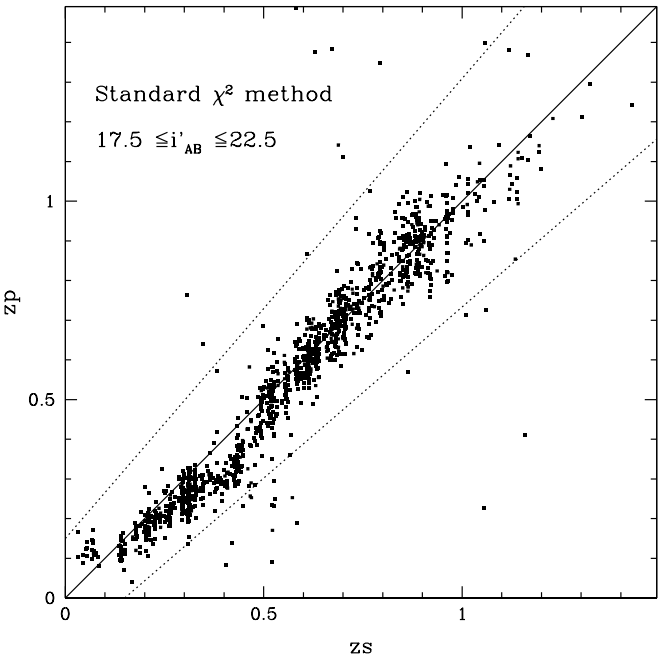

Fig. 3. Comparison between spectroscopic and photometric redshifts obtained with the standard χ^2 method (without adding the spectroscopic information) for a bright selected sample $17.5 \leq i'_{AB} \leq 22.5$.

4.1. Systematic offsets

We select a control sample of 468 very bright galaxies ($i'_{AB} \leq 21.5$) with a spectroscopic redshift. Using a χ^2 minimization (equation 1) at fixed redshift, we determine for each galaxy the best-fit CWW template. We note F^f_{obs} the observed flux in the filter f and F^f_{pred} the predicted flux derived from the best-fit template. For each filter f, we minimize the sum

$$\psi^2 = \sum_{i' \leq 21.5}^{Ngal} \left((F^f_{\rm pred} - F^f_{\rm obs} + s^f)/\sigma^f_{\rm obs} \right)^2$$

leaving s^f as a free parameter. For normal uncertainties in the flux measurement, the average deviation s^f should be 0. Instead, we observe some systematic differences which are listed in Table 1. These differences never exceed 0.1 magnitude and have an average value of 0.042 magnitude. They depend weakly on the magnitude cut adopted to select the bright sub-sample (Table 1) and are also weakly depending on the set of templates (see Table 1 with the values obtained using the synthetic library PEGASE Fioc & Rocca-Volmerange 1997). Uncertainties in the calibration of the photometric zero-points may create discontinuities not reproduced by the templates. The size of these systematic differences are compatible with the expected uncertainties in the absolute zero-point calibration (0.05 magnitudes).

We then proceed to correct the predicted apparent magnitudes from these systematic differences. s^f is the estimated correction that we apply to the apparent mag-

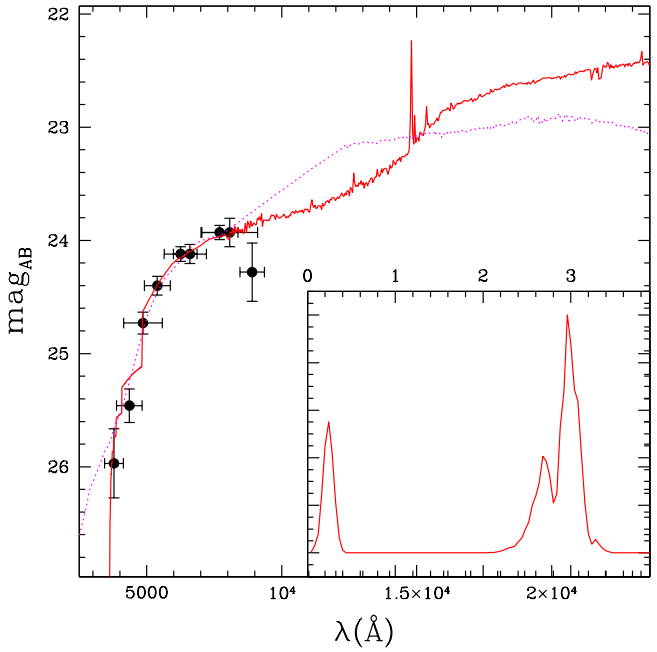

Fig. 4. Example of best-fitted templates on multi-color data for a galaxy at $zs = 0.311$. The solid black points correspond to the apparent magnitudes in the $u^*, B, g', V, r', R, i', I, z'$ filters from the left to the right respectively. The solid line corresponds to a template redshifted at $zp = 2.97$ and the dotted line at $zp = 0.24$. The enclosed panel is the associated Probability Distribution Function (PDFz).

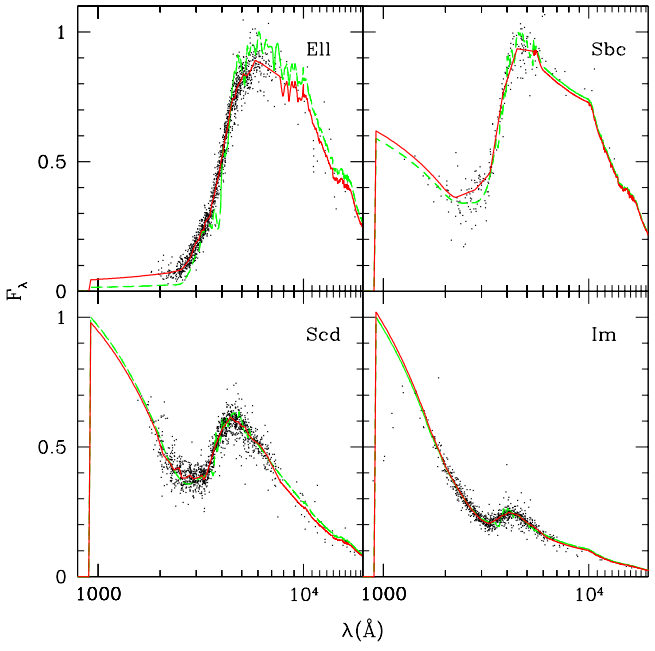

Fig. 5. Each panel corresponds to one of the 4 CWW templates (Ell, Sbc, Scd, Irr). The points correspond to the flux of each galaxy redshifted to the rest-frame using the spectroscopic redshifts. The green dashed lines are the initial SEDs and the red solid lines are the optimized SEDs.

nitudes in a given filter f. If we repeat a second time the procedure of template-fitting after having adjusted the zero-points, the best-fit templates may change. We check that the process is converging: after three iterations the estimated corrections s^f vary less than 2%. The values listed in the Table 1 are measured after 3 iterations and are used to correct the apparent magnitudes. Since the uncertainties in the zero-point calibration are not better than 0.01, we add 0.01 in quadrature to the apparent magnitude errors.

4.2. Template optimization

The apparent magnitude measured in the filter λ_{eff} provides the rest-frame flux at $\lambda_{eff}/(1+z_i)$ for a galaxy with a spectroscopic redshift z_i. Since all the galaxies are at different redshifts, we can estimate the rest-frame flux over a continuous range of rest-frame wavelengths from the spectroscopic sample. Using this property, we optimize our set of CWW templates.

We split the galaxy spectroscopic sample according to the best-fit template (4 CWW + a starburst template with a possible additional extinction). Keeping only the objects fitted without additional extinction, we use a subsample of 309 galaxies to optimize the templates. The black points in Fig.5 show the rest-frame flux reconstructed from observed apparent magnitudes. We observe a slight deviation between these points and the initial templates (dashed lines), particularly for early spectral type galaxies. We sort the rest-frame flux according to their wavelengths and bin them by group of 50 points. To produce the optimized templates, we connect the median flux in each bin (solid lines). When no data are available, we keep the extrapolation provided by the initial set of templates. We don't optimize the starburst template to conserve emission lines.

The colors predicted for these 5 main optimized templates are shown as a function of redshift in Fig.2. The

filter	CWW $i'_{AB} < 20.5$	CWW $i'_{AB} < 21.5$	CWW $i'_{AB} < 22.5$	PEGASE $i'_{AB} < 21.5$
u^*	+0.044	+0.045	+0.041	+0.066
g'	-0.080	-0.080	-0.079	-0.087
r'	+0.011	-0.006	-0.012	-0.002
i'	-0.005	-0.002	-0.004	-0.001
z'	-0.037	-0.025	-0.014	-0.045
B	+0.057	+0.067	+0.074	+0.063
V	-0.066	-0.062	-0.059	-0.066
R	+0.098	+0.086	+0.083	+0.096
I	-0.022	-0.001	-0.002	-0.012

Table 1. Systematic differences s^f between observed and predicted apparent magnitudes. These values are given for the set of CWW templates and for different cuts in apparent magnitudes. We add also the values obtained with the synthetic library PEGASE. Throughout the paper, we use the values quoted for CWW $i'_{AB} < 21.5$.

observed trend in the color-z relation are well reproduced by our set of templates. For $r'-i'$ and $i'-z'$ colors, we observe oscillations of the predicted color-z relation for the starburst template. These oscillations are explained by the contribution of emission lines like H_α and OIII to the observed flux. Since we use only one starburst template to restrain the possible degeneracies in the color-z space, we are not covering the broad range of possible intensities and line ratios. In particular, we are not reproducing some blue observed colors $(r'-i')_{AB} < 0.1$ and $(i'-z')_{AB} < 0$ (Fig.2). This lack of representativity, adopted voluntary to avoid degeneracies, leads to an accretion of photometric redshifts in the peaks of the color-z relation. The consequence is the presence of narrow peaks in the redshift distribution for the starburst spectral types.

Finally, these 5 main optimized templates are linearly interpolated in a total of 62 templates to improve the sampling of the redshift-color space and then the accuracy of the redshift measurement.

4.3. Bayesian approach

The Bayesian approach (Benítez 2000) allows us to introduce a relevant *a priori* information in the PDFz. Following the formalism developed by Benítez (2000), we introduce the prior

$$p(z,T|i'_{AB}) \propto p(T|i'_{AB})p(z|T,i'_{AB}) \quad (2)$$

with $p(z|T,i'_{AB})$ the redshift distribution and $p(T|i'_{AB})$ the probability to observe a galaxy with the spectral type T. $p(z|T,i'_{AB})$ is parametrized as:

$$p(z|T,i'_{AB}) \propto z^{\alpha_t} exp\left(-\left[\frac{z}{z_{0t}+k_{mt}(i'_{AB}-20)}\right]^{\alpha_t}\right), \quad (3)$$

and $p(T|i'_{AB})$ as:

$$p(T|i'_{AB}) = f_t e^{-k_t(i'_{AB}-20)}. \quad (4)$$

The subscript t shows the dependency on the type. Using the formalism from Benítez (2000), we recompute the values of the free parameters using the VVDS redshift distribution. We split the sample according to the 4 optimized CWW templates. We adjust the parameters α_t, z_{0t}, k_{mt} to maximize the likelihood to observe the VVDS spectroscopic sample. We use the MINUIT package of the CERN library (James & Roos 1995) to perform the maximization (MIGRAD procedure) and to obtain the corresponding errors (MINOS procedure). The values of these parameters for each type are given in Table 2. The parameters f_t and k_t are also given in Table 2 for types 1, 2, 3 and the fraction of type 4 is automatically set to complete the sample.

4.4. Summary

The photometric redshifts are estimated using the code *Le_Phare* (Arnouts & Ilbert). We calibrate the standard χ^2 method using the VVDS spectroscopic redshifts:

- We first adjust iteratively the zero-points of the multi-color catalogue using a bright spectroscopic sample.
- Then we optimize our primary set of templates taking back the observed flux in rest-frame flux.
- Finally we apply a prior based on the VVDS redshift distribution following the Bayesian formalism from Benítez (2000).

5. Results: accuracy of the photometric redshifts

Comparing the spectroscopic and photometric redshift samples on the CFHTLS-D1, we assess the quality of the photometric redshifts obtained with the calibration method described in section 4.

5.1. Method improvement

Fig.6 shows the photometric redshifts versus the spectroscopic redshifts for different steps in the calibration method. The systematic trends observed with the standard χ^2 method (top left panel, method *a)*) are removed by the template optimization and the systematic offset corrections (top right panel, method *b)*). After this step, the accuracy reaches $\sigma_{\Delta z/(1+zs)} = 0.037$. Adding a prior on the redshift distribution decreases the fraction of catastrophic errors without creating any systematic trends (bottom left panel, method *c)*). The final fraction of catastrophic errors has decreased by a factor 2.3. In the following, we restrict our analysis to the best method *c)*. This comparison shows the essential role of the spectroscopic information to build a robust photometric redshift sample.

With our final calibration method, we reach an accuracy $\sigma_{\Delta z/(1+zs)} = 0.037$. At $i'_{AB} \leq 24$, we recover 96% of the galaxies in the redshift range $|\Delta z| < 0.15(1+zs)$. $\sigma_{\Delta z/(1+zs)} = 0.037$ is similar to the accuracy obtained by the COMBO-17 survey with a larger set of medium band filters (Wolf et al. 2004). However, considerations on the quality of photometric redshifts derived from statistical measurements using the whole sample are not really meaningful since it depends on the apparent magnitude, the spectral type and the redshift range. We investigate these dependencies in the next section.

5.2. Dependency on apparent magnitude, type and redshift

Fig.7 shows the comparison between photometric and spectroscopic redshifts as a function of apparent magnitude. The fraction of catastrophic errors η increases by a factor 12 going from $17.5 \leq i'_{AB} \leq 21.5$ up to $23.5 \leq i'_{AB} \leq 24$. The redshift rms increases continuously from $\sigma_{\Delta z/(1+zs)} \sim 0.028$ up to $\sigma_{\Delta z/(1+zs)} \sim 0.048$. The apparent magnitude is therefore a key parameter, as expected since the template-fitting is less constrained for the fainter objects.

Fig.8 shows the comparison between photometric and spectroscopic redshifts as a function of the spectral type.

spectral type	α_t	z_{0t}	k_{mt}	f_t	k_t
Ell	$3.331^{+0.109}_{-0.108}$	$0.452^{+0.015}_{-0.015}$	$0.137^{+0.007}_{-0.007}$	$0.432^{+0.047}_{-0.047}$	$0.471^{+0.043}_{-0.043}$
Sbc	$1.428^{+0.081}_{-0.080}$	$0.166^{+0.024}_{-0.023}$	$0.129^{+0.013}_{-0.013}$	$0.080^{+0.021}_{-0.021}$	$0.306^{+0.098}_{-0.098}$
Scd	$1.583^{+0.038}_{-0.038}$	$0.211^{+0.015}_{-0.014}$	$0.140^{+0.006}_{-0.006}$	$0.312^{+0.033}_{-0.033}$	$0.127^{+0.036}_{-0.036}$
Irr	$1.345^{+0.021}_{-0.021}$	$0.204^{+0.014}_{-0.014}$	$0.138^{+0.005}_{-0.005}$	...	...

Table 2. Parameters used for the prior $P(z,T|i'_{AB})$ using the formalism from Benítez (2000). These parameters are derived from the VVDS spectroscopic sample.

We define the spectral type according to the best-fit template. The fraction of catastrophic errors η increases by a factor 7 from the elliptical to the starburst spectral types. The starburst galaxies represent 18% of the spectroscopic sample but 54% of the catastrophic errors. The accuracy in the redshift measurement is similar for the Ell, Sbc, Scd and Irr spectral types with $\sigma_{\Delta z/(1+zs)} = 0.032 - 0.036$ but raises to $\sigma_{\Delta z/(1+zs)} = 0.047$ for the starburst galaxies. Such a dependency on the spectral type is expected since the robustness of the photometric redshifts relies strongly on the Balmer break, less marked for the latest type. In addition, the photometric redshift estimate of late spectral type galaxies is affected by the intrinsic dispersion in the properties of the emission lines and by the large range in intrinsic extinction.

The photometric redshift reliability also depends on the considered redshift range. We quantify the dependency to the redshift in Fig.9 and Fig.10 showing the rms scatter $\sigma_{\Delta z/(1+zs)}$ and the fraction of catastrophic errors η as a function of redshift up to $z = 1.5$. We split the sample into a bright $17.5 \leq i'_{AB} \leq 22.5$ and a faint $22.5 \leq i'_{AB} \leq 24$. We choose the limit $i'_{AB} = 22.5$ since it corresponds to the depth of the shallow VVDS and zCOSMOS spectroscopic surveys. The fraction of catastrophic errors increases dramatically only at $z < 0.2$. At $0.2 \leq z \leq 1.5$, the accuracy remains always better than $0.045(1+zs)/0.55(1+zs)$ for the bright/faint sample respectively. The fraction of catastrophic errors η remains always less than $\sim 4\%/14\%$ for the bright/faint sample respectively (Fig.10). We observe a degeneracy for $zs < 0.4$ and $1.5 < zp < 3$ faint galaxies (bottom left panel of Fig.6). The origin of this degeneracy is a mismatch between the Balmer break and the intergalactic Lyman-alpha forest depression at $\lambda < 1216$Å. 70% of the galaxies at $1.5 < zp < 3$ are in fact at $zs < 0.4$ which prevents from the use of this spectral range. At $zs > 3$, the Lyman Break is observed between the u^* band and the g' bands, allowing a reliable photometric redshift estimate for Lyman Break galaxies. We recover 6 of the 8 galaxies at $zs > 3$ (bottom left panel of Fig.6). Even if the quality of the photometric redshifts appears good, we point out that we are using only spectroscopic redshifts with the highest confidence level which is a specific population easier to isolate both in photometry and in spectroscopy since they have a significant Lyman break (Le Fèvre et al. 2005b). Moreover, we have tuned the calibration method to be efficient at $z < 1.5$ using a prior

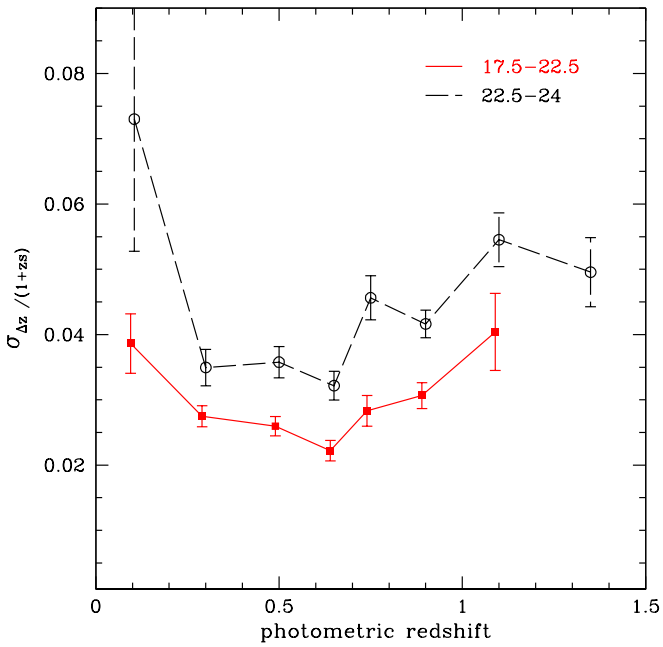

Fig. 9. Accuracy of the photometric redshifts as a function of redshift. Catastrophic errors are removed from the sample. Only bins with more than 10 objects are shown.

on the redshift distribution (see section 4.3) and without allowing galaxies to be brighter than $M_{B_{AB}} = -24$ (Ilbert et al. 2005). We finally conclude that the most appropriate redshift range for forthcoming scientific analysis is $0.2 < zp < 1.5$.

5.3. Error analysis

We investigate here the reliability of the error associated to the photometric redshift estimate.

The redshift Probability Distribution Function (PDFz) (see Arnouts et al. 2002) is directly derived from the χ^2 distribution

$$PDFz = B \exp\left(-\frac{\chi^2(z)}{2}\right), \quad (5)$$

with B a normalization factor. *Le_Phare* (Arnouts & Ilbert) produces the PDFz for each object. A second redshift solution is likely when a second peak is detected in the PDFz above a given threshold. An example of galaxy

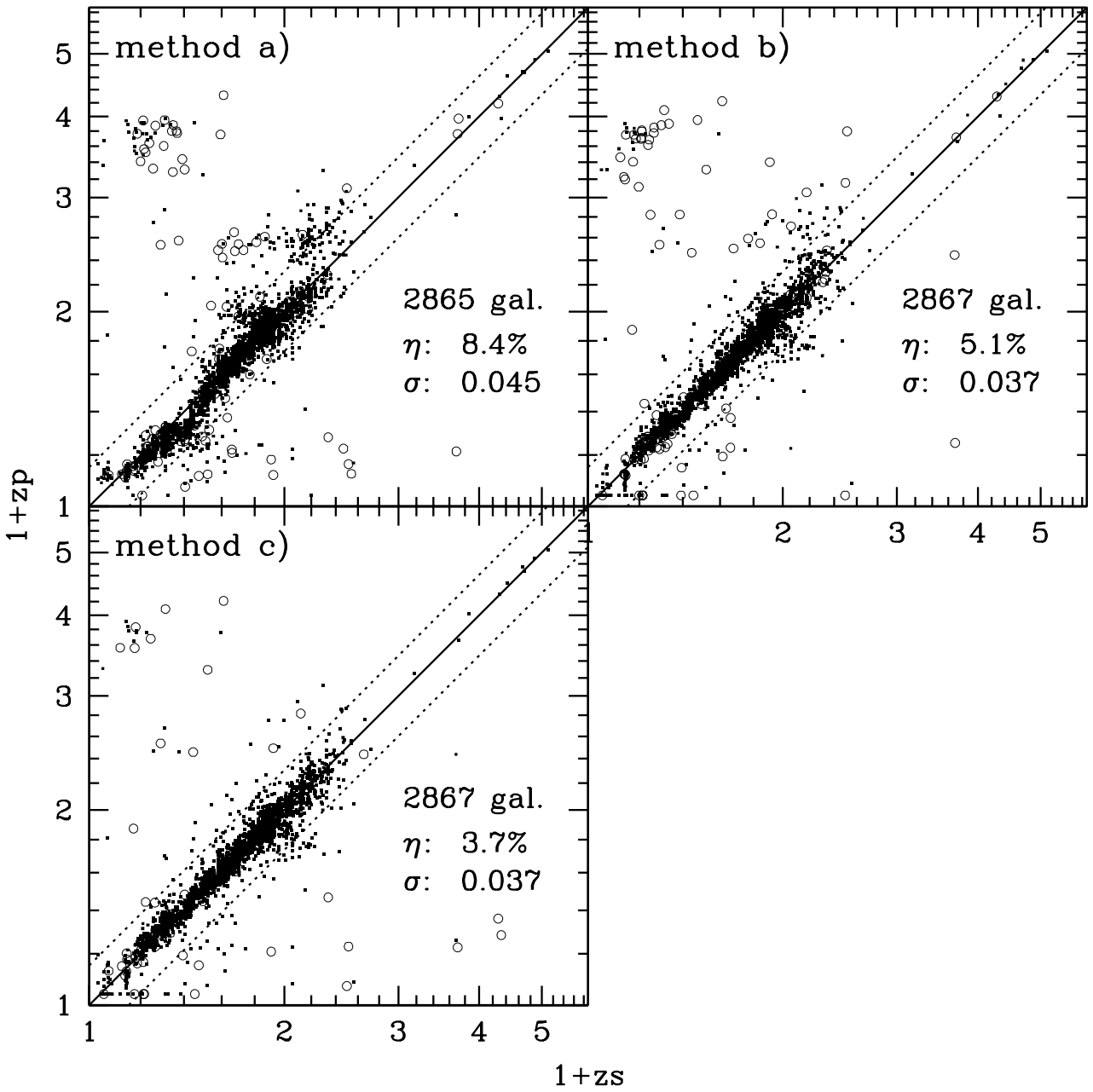

Fig. 6. Photometric redshifts versus spectroscopic redshifts for the sample $17.5 < i'_{AB} < 24$. Each panel corresponds to an additional step in the calibration method with: *method a*) the standard χ^2 method ; *method b*) adding the templates optimization and the corrections of the systematic offsets ; *method c*) our best method using the Bayesian approach, the templates optimization and the corrections of systematic offsets. The solid line corresponds to $zp = zs$. The dotted lines are for $zp = zs \pm 0.15(1+zs)$. We quote as catastrophic errors the fraction η of galaxies with $|zs - zp|/(1+zs) > 0.15$ and the accuracy $\sigma_{\Delta z/(1+zs)}$. The open symbols correspond to galaxies with a second peak detected in the PDFz (probability threshold at 5%).

with the good redshift solution enclosed in the second peak of the PDFz is shown in Fig.4. The galaxies with second peak in the PDFz are flagged with open circles in Fig.6, Fig.7, Fig.8 and composed a large fraction of the catastrophic errors. We find that the fraction of catastrophic errors increases drastically in those cases: when a second peak is detected with a probability greater than 5% the fraction of catastrophic errors increases to $\eta = 42\%$. Removing these galaxies from the sample could be useful to select a more robust subsample.

The error bars on the photometric redshifts are given by $\chi^2(z) = \chi^2_{min} + \Delta\chi^2$. $\Delta\chi^2 = 1$ and $\Delta\chi^2 = 9$ are used to compute the error bars at 1σ and 3σ respectively. Fig.11 shows the estimated error bars at 3σ in small bins of apparent magnitudes. The size of the error bar increases toward faint apparent magnitudes, in a consistent way with

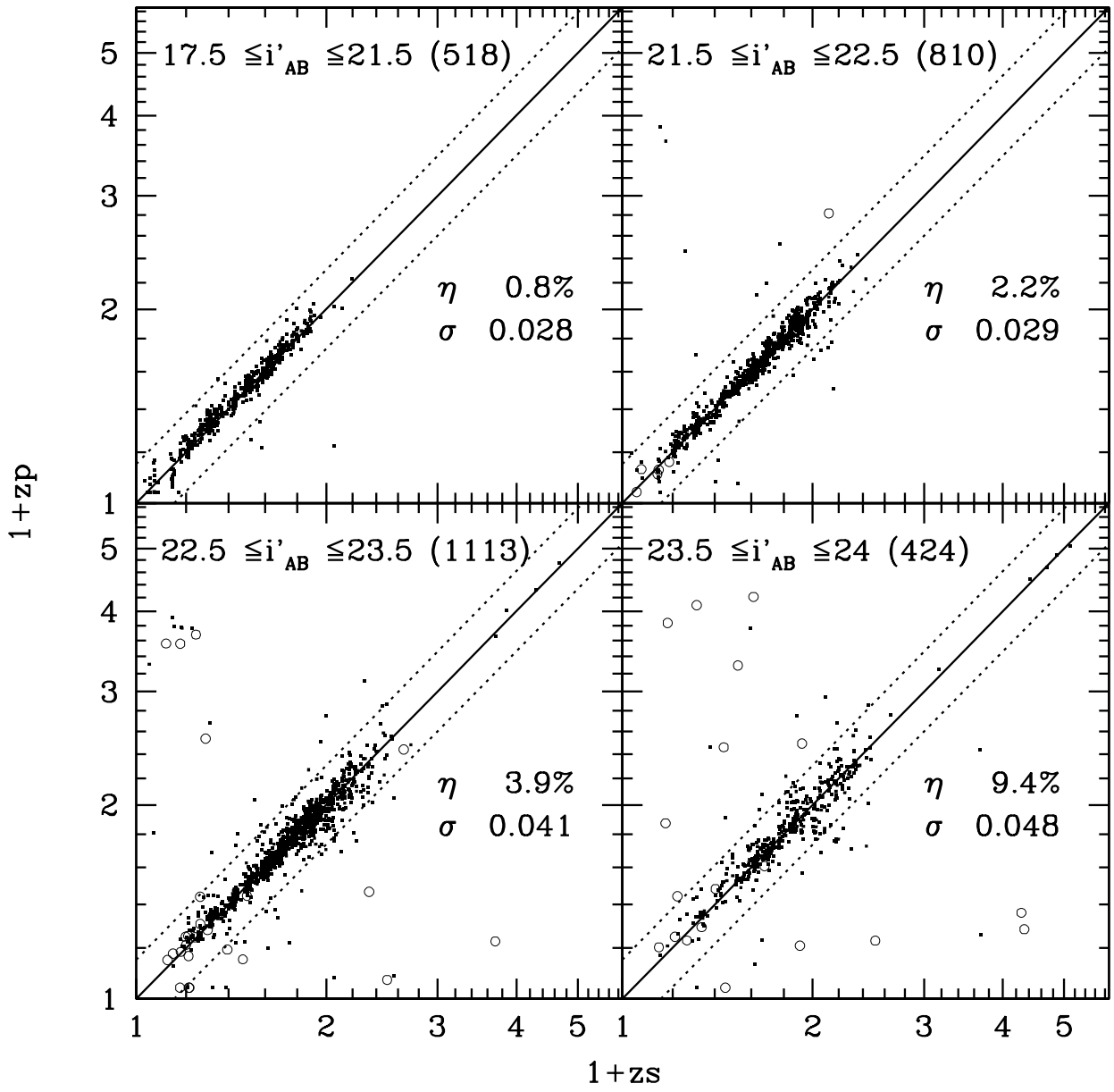

Fig. 7. Same as Fig.6 with the final calibration method *c)*. Each panel corresponds to a different selection in apparent magnitude.

the Δz rms. We find that 67% and 90% of the spectroscopic redshifts are well located in the 1σ and 3σ error bars respectively. We note that these values remain lower than the theoretical values since uncertainties linked to the photometry (blending, bright neighbor) or to the templates representativity are not taken into account in the PDFz. We conclude that our 1σ error bars are well representative of the photometric redshift quality, which will be useful to assess their accuracy beyond the spectroscopic limits.

5.4. Comparison between photometric and spectroscopic redshift distributions

In order to present the galaxy redshift distribution, we first need to remove the stars from the sample. We use a morphological criterion which is the half-light radius $r_{1/2}$ measured with SExtractor (Bertin & Arnouts 1996). From the spectroscopic sample, we find that 95% of the stars have $r_{1/2} < 2.7$. Since 16% of the galaxies have also $r_{1/2} < 2.7$, we combine this morphological criterion with a color criterion. For each object, we compute simultaneously the χ^2 for the galaxy library and the χ^2_s for the star library (Pickles 1998). If the conditions $\chi^2 - \chi^2_s > 0$

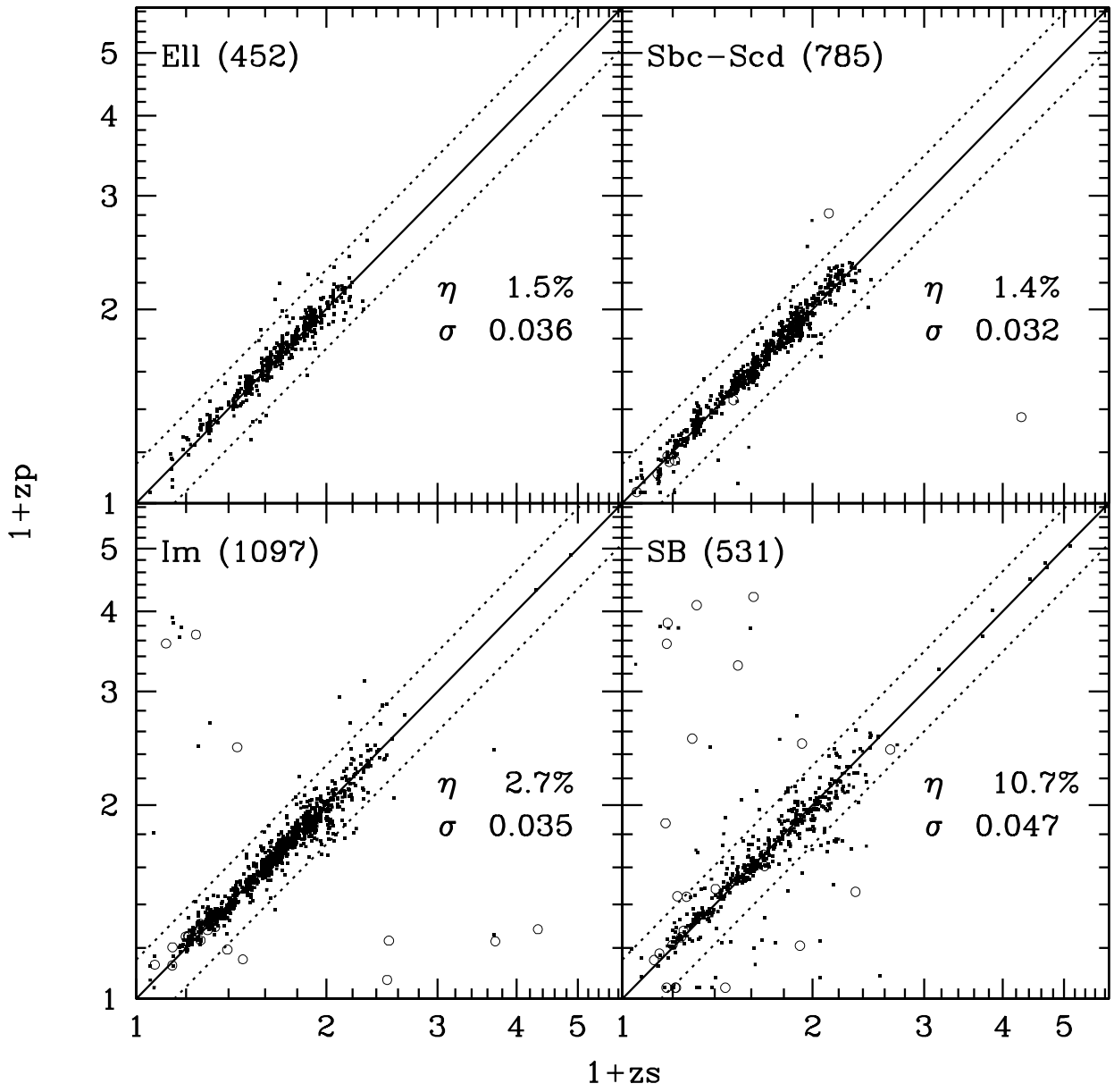

Fig. 8. Same as Fig.6 with our final calibration method *c)*. The sample is selected at $17.5 \leq i'_{AB} \leq 24$. Each panel corresponds to a different selection in spectral type defined according to the best-fit template.

and $r_{1/2} < 2.7$ are satisfied simultaneously, the object is flagged as a star. Applying these criteria on the spectroscopic sample, we recover 79% of the stars and only 0.77% galaxies are misclassified as stars. The remaining 21% of stars are misclassified as galaxies and 69% contaminate the redshift range $zp < 0.2$.

Since we use the spectroscopic redshift distribution as a prior (see section 4.3) a critical point is to check at which level the photometric redshift distribution depends on the prior. We compare the redshift distributions obtained using the prior (weighted solid lines) and without (dashed lines) in Fig.12. The prior has no impact on the global shape of the redshift distribution. We see significant differences in the redshift distributions at $z > 2$, when the prior remove efficiently the catastrophic failures at $2 < zp < 3$.

For the $i'_{AB} \leq 23$ and the $i'_{AB} \leq 24$ selected samples, we compare in Fig.12 the photometric and the VVDS spectroscopic redshift distributions. The distributions are in excellent agreement up to $z \sim 1.5$. At $1.5 < z < 3$, the photometric redshifts are contaminated by low redshift galaxies (see section 5.2) and few spectral features can support a spectroscopic redshift measurement (Le Fèvre et al. 2005a). Both effects explain the difference

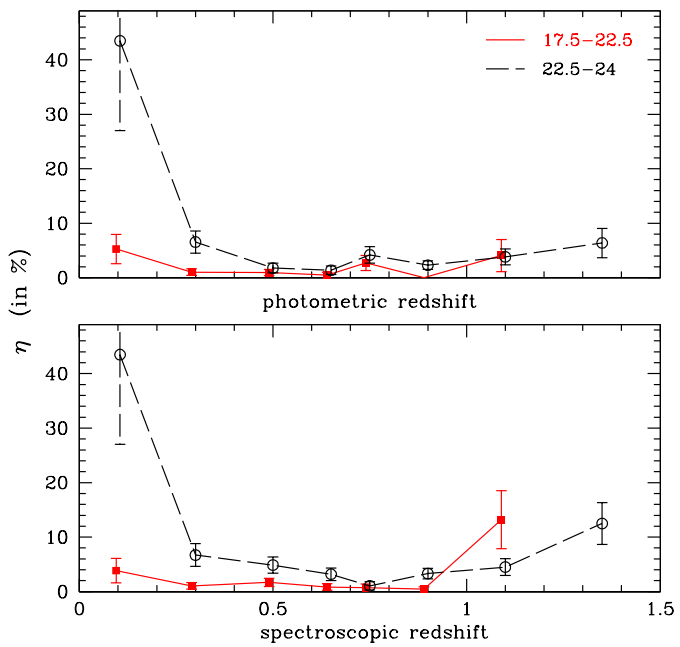

Fig. 10. Fraction of catastrophic errors η per redshift bins. The catastrophic errors are defined as galaxies with $|zs - zp|/(1 + zs) > 0.15$. The fraction is measured as a function of the photometric redshift (top panel) and of the spectroscopic redshift (bottom panel). The top panel shows the level of contamination, i.e. the fraction of wrong redshifts in a given photometric redshift slice. The bottom panel shows the level of incompleteness, i.e. the fraction of redshifts not recovered in a given photometric redshift slice. Only bins with more than 10 objects are shown.

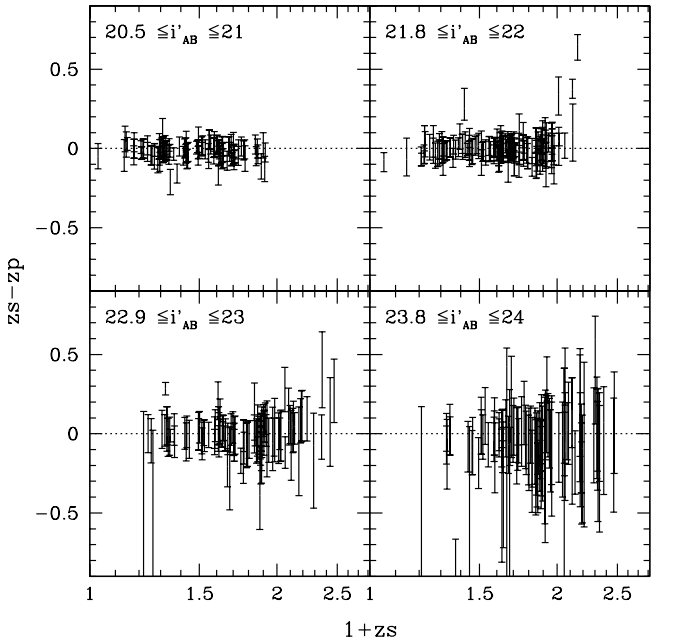

Fig. 11. Δz as a function of redshift in 4 small apparent magnitude bins (for the clarity of the figure). We report the 3σ error bars on the photometric redshift estimate.

between the photometric and spectroscopic redshift distribution at $z > 1.5$.

We recover clear peaks present both in the photometric and spectroscopic redshift distributions. We smooth the spectroscopic and photometric redshift distributions using a step $\Delta z = 0.2$ and a sliding window. The ratio between the observed redshift distribution obtained with a step $\Delta z = 0.01$ and the smoothed redshift distribution shows three peaks at $zp \sim 0.31, 0.61, 0.88$ in the photometric redshift distribution, corresponding to peaks identified at $zs \sim 0.33, 0.60, 0.89$ in the spectroscopic redshift distribution. The significance of the detection is lower by a factor 2 in the photometric redshift sample since the peaks are broadened by the uncertainties on the photometric redshift estimates.

6. Added value of each multi-color data set

For analysis specific to each survey (VVDS and CFHTLS), we characterize the reliability of the photometric redshifts for each data set. In addition, we discuss the added value of the different filters.

6.1. Added value of u^* and z' bands

Removing successively the u^* and the z' bands, we show possible systematic trends if these bands are not available or if they are shallower.

Fig.13 (top left panel) shows the photometric redshifts computed without u^* band data. Only $\sim 70\%$ of the photometric redshifts at $zs < 0.4$ are recovered, to be compared with $\sim 90\%$ using the u^* band. Since the filter system is no longer sensitive to the Lyman break, a large fraction of low redshift galaxies contaminates the $zp > 3$ redshift range. This test shows the importance of a deep u^* band to constrain the photometric redshifts at $z < 0.4$ and $z > 3$.

Fig.13 (top right panel) shows the photometric redshifts computed without z^* band data. Most of the photometric redshifts at $zs > 1$ are estimated at $zp \leq 1$. We observe an accumulation of photometric redshifts around $zp \sim 0.8 - 0.9$. This trend is expected since the filter system is no longer sensitive to the Balmer break at $z > 1$. Then, the use of the photometric redshifts is problematic even at $z < 1$ without z' band data.

6.2. Photometric redshifts from the VVDS imaging survey alone

The VVDS multi-color survey is conducted in the B, V, R and I bands over 10 deg^2 (Le Fèvre et al. 2004a). The accuracy of the photometric redshifts using only BVRI is presented in Fig.13 (bottom right panel). Since the VVDS photometric survey is shallower, the quality of the photometric redshifts is obviously worse than the results presented previously. η raises at 19.1% which is a factor 5 greater than our best value. As we show in section 6.3, the absence of deep u^* and z' band data explains the difficulty

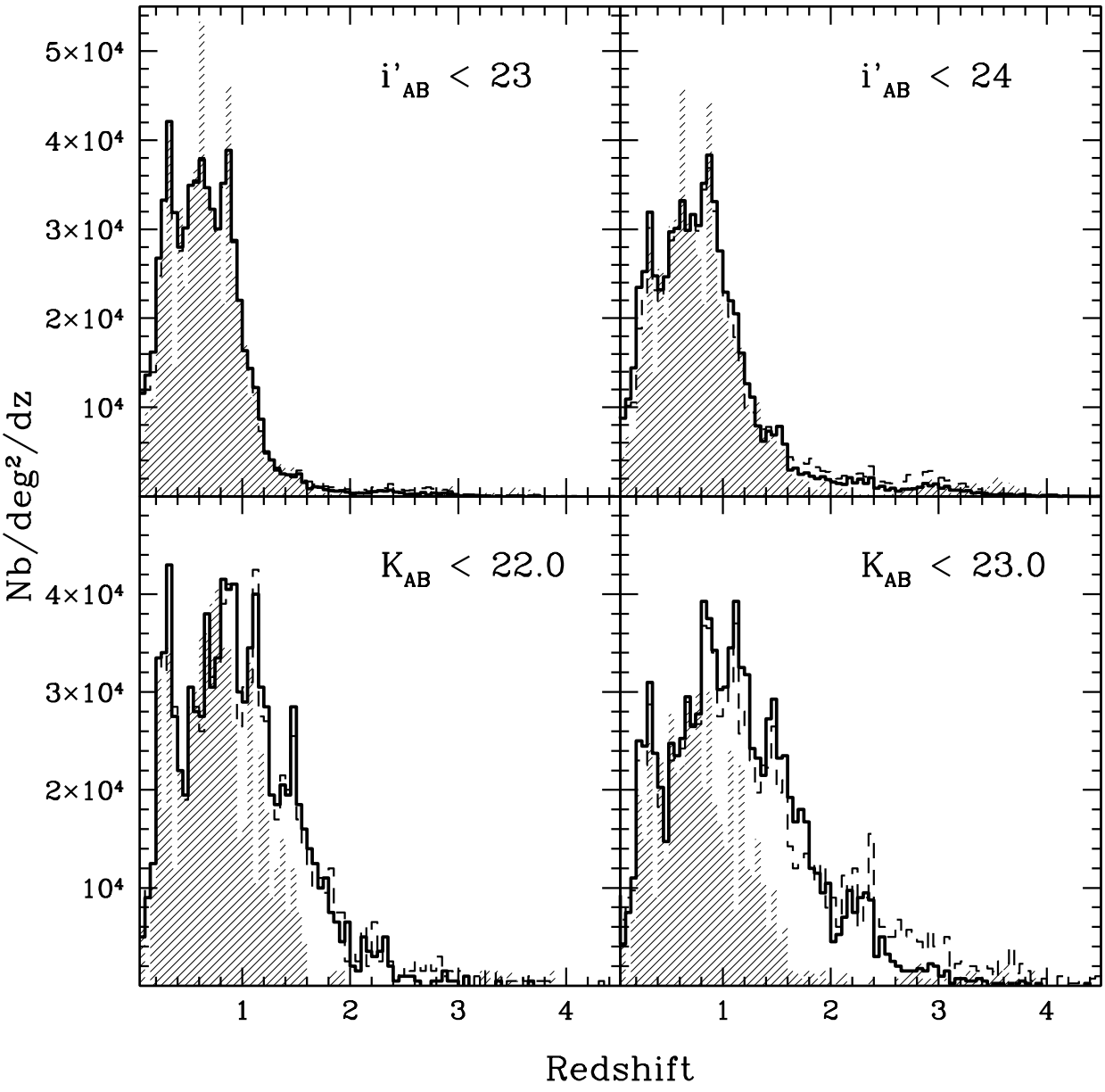

Fig. 12. Comparison between the photometric redshift distributions and the VVDS spectroscopic redshift distributions on the CFHTLS-D1 field, for samples selected at $i'_{AB} < 23$ (top left), $i'_{AB} < 24$ (top right), $K_{AB} < 22$ (bottom left) and $K_{AB} < 23$ (bottom right). The solid lines and the dashed lines correspond respectively to the estimate with and without using the prior on the redshift distribution. These distributions are compared with the spectroscopic redshift distributions (shaded histograms) from the VVDS sample, originally selected at $I_{AB} \leq 24$. To keep the same vertical axis, the redshifts distributions are divided by a factor 2 for $i' \leq 24$, $K \leq 23$.

to recover redshifts at $zs < 0.4$ and $zs > 1$. However, even using only 4 broad bands, we recover 80% of the spectroscopic redshifts at $I_{AB} \leq 24$ with $\sigma_{|\Delta z|/(1+zs)} = 0.057$.

6.3. Photometric redshifts from the CFHTLS imaging data alone

The deep CFHTLS survey consists in four fields imaged over 3.11 deg^2 in the u^*, g', r', i', z' filters. The quality of the photometric redshifts computed using only the u^*, g', r', i', z' bands is presented in Fig.14 (top panel) for the CFHTLS-D1. We find $\eta = 4.2\%$ and $\sigma_{|\Delta z|/(1+zs)} = 0.040$. These CFHTLS photometric redshifts are already close to our best value using the full photometric dataset. Photometric redshifts on the other CFHTLS deep fields will be introduced in section 7.

Magnitude cut	$i^* \leq 23$	$i^* \leq 24$	$Ks \leq 22$	$Ks \leq 23$
z_m	0.76	0.90	0.90	1.07
% at $z > 1$	13%	28%	28%	43%

Table 3. Median redshifts and fraction of galaxies at $z > 1$ for samples selected according to $i'_{AB} \leq 23, 24$ and $K_{AB} \leq 22, 23$ in the CFHTLS-D1

	D1	D2	D3	D4
$17.5 < i'_{AB} < 22$	0.49	0.48	0.49	0.48
$22 < i'_{AB} < 23$	0.75	0.75	0.75	0.81
$23 < i'_{AB} < 24$	0.89	0.86	0.86	0.95
$24 < i'_{AB} < 25$	1.00	0.95	0.94	1.03

Table 4. Median redshifts in the 4 CFHTLS deep fields (columns) for samples selected according to $17.5 < i'_{AB} < 22$, $22 < i'_{AB} < 23$, $23 < i'_{AB} < 24$, $24 < i'_{AB} < 25$ from the top to the bottom, respectively.

6.4. The NIR sample

Deep NIR observations in the J and K bands are available for 160 arcmin^2 (Iovino et al. 2005) sub-area of the D1 field. This complete subsample of 3688 galaxies at $K_{AB} \leq 23$ represents a unique dataset in term of depth and area (1 magnitude deeper on a 3 times larger area than the K20 survey, Cimatti et al. 2002). The NIR is crucial to constrain the photometric redshifts in the 'redshift desert' since the J band is sensitive to the Balmer break up to $z \sim 2.5$ and enters in the K band at $z > 3.8$. The photometric redshifts for galaxies selected at $K_{AB} < 23$ are shown in Fig.13 (bottom left panel). We obtain the most reliable photometric redshifts on this subsample with $\eta = 2.1\%$ and $\sigma_{|\Delta z|/(1+zs)} = 0.035$.

We present in Fig.12 the redshift distributions for samples selected according to $K_{AB} \leq 22, 23$. Comparing the photometric and spectroscopic redshift distributions, we observe a large difference at high redshift tail explained by the color incompleteness created in the spectroscopic sample by the $I_{AB} \leq 24$ selection. The median redshifts and the fraction of galaxies with $z > 1$ are given in Table 3. We observe that near-infrared selected samples are more efficient to target a high redshift population than i' selected sample. We find 43% of the galaxies at $z > 1$ for a sample selected at $K_{AB} \leq 23$. As previous K selected surveys (Cimatti et al. 2002, Somerville et al. 2004), we find a large population of galaxies at $z > 1$.

7. Photometric redshifts in the CFHTLS "Deep Fields" D1, D2, D3 and D4

We finally apply the calibration of photometric redshifts derived from the CFHTLS-D1 field and the VVDS spectroscopic sample on the 4 CFHTLS "Deep Fields". The imaging data used in this paper corresponds to the 'T03' release of the CFHTLS.

The three CFHTLS deep fields D2, D3, D4 are imaged with the same instrument and are reduced homogeneously (McCracken et al. 2006, in preparation). We therefore assume that we can measure the photometric redshifts using the same method for these three fields. As a consistency check, we use the 364 spectroscopic redshifts from the DEEP1 survey publicly available in the CFHTLS-D3 field (Phillips et al. 1997). This allows to test blindly the quality of these photometric redshifts without any additional calibration. The comparison is shown in the bottom panel of Fig.14. We find $\eta = 3.8\%$ and $\sigma_{|\Delta z|/(1+zs)} = 0.035$ at $i'_{AB} \leq 24$ and $z < 1.5$, without any systematic trend. We therefore conclude that our calibration method derived from D1 can be applied to the other CFHTLS deep fields.

The quality reaches by the photometric redshifts using only the u^*, g', r', i', z' is already shown in section 6.3, but only in the CFHTLS-D1 field and for $i'_{AB} \leq 24$. Since we have already demonstrated in Section 5.3 that the 1σ error bars are well representative of a measurement at 68% of confidence level, we use the 1σ error bars to quantify the accuracy of the photometric redshifts in the different fields and beyond the spectroscopic limit. Fig.15 shows the fraction of photometric redshifts with a 1σ error bar left than $0.15 \times (1 + z)$. The best constraint is obtained on the CFHTLS-D1 field and gradually declines for the D4, D3 and D2. The constraint on the photometric redshifts is the lowest on the D2, which is expected since the total exposure times in the u^* and z' bands are respectively 7.7 and 1.7 times lower for the D2 field than for the the D1 field. We note that the specific trends described in section 6.1 and shown in Fig.13 could partially affect the photometric redshift estimates for the CFHTLS-D2 given than this field has substantially shallower u^* and z' data. The other significant trends observed in Fig.15 are expected from our previous comparisons:

- the redshift range $0.2 < z \leq 1.5$ is the most suitable for the 4 fields which is expected since this redshift range is determined by the set of filters used.
- the accuracy of the photometric redshifts decreases toward fainter apparent magnitudes, faster at $i'_{AB} > 24$. For $0.2 < z < 1.5$, the fraction of galaxies with $\sigma_{zp}(68\%) > 0.15 \times (1+z)$ remains greater than $\sim 80\%$ at $i'_{AB} = 25$ in the CFHTLS-D1 field.

We show in Fig.16 the redshift distributions obtained in the 4 CFHTLS deep fields. As expected, the median redshift increases toward fainter sample (Table 4) going from $z_m \sim 0.45$ at $i'_{AB} \leq 22$ to $z \sim 1$ at $24 \leq i'_{AB} \leq 25$. The median redshift are in good agreement between the

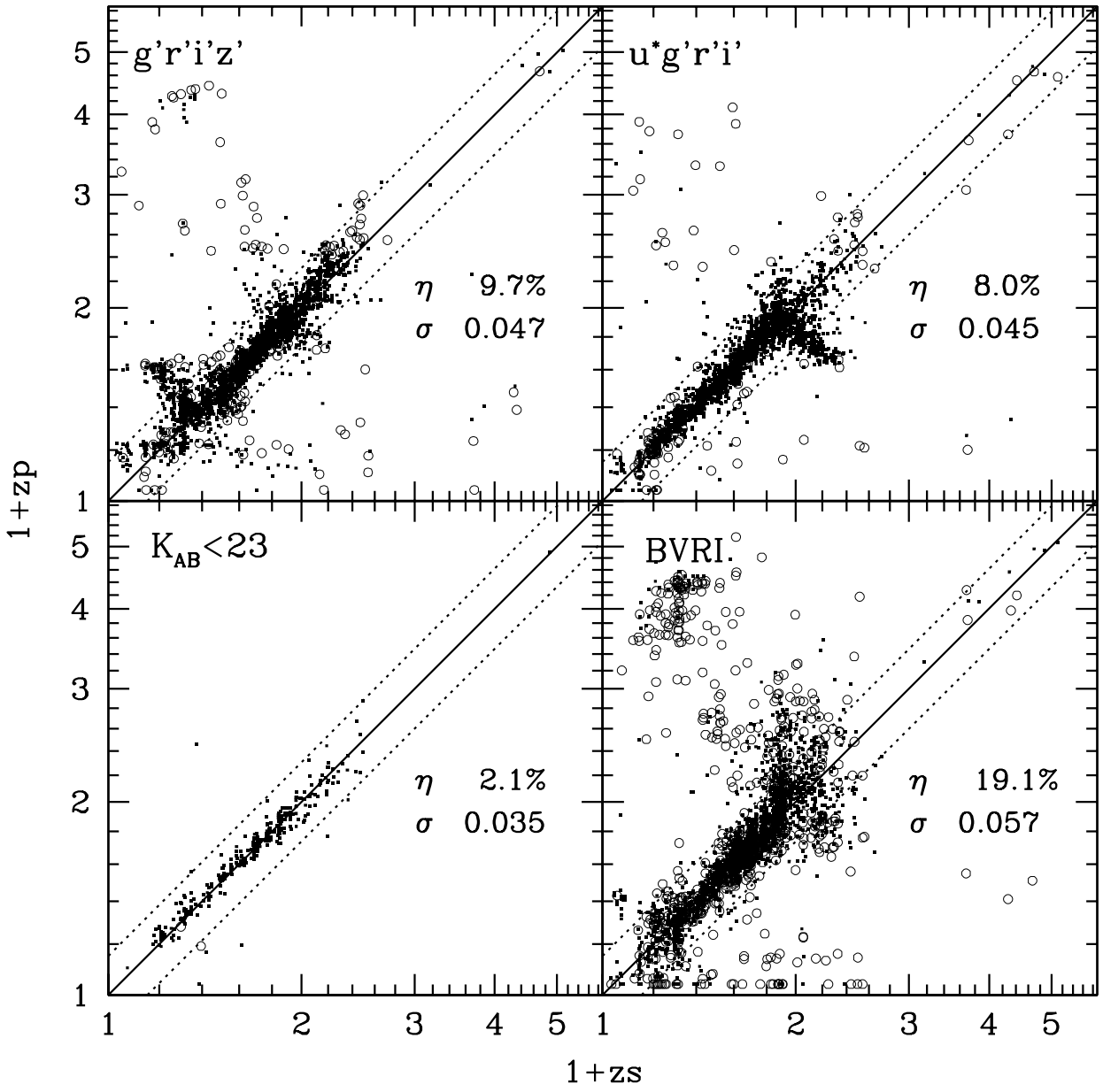

Fig. 13. Comparison between spectroscopic and photometric redshifts for different combinations of filters. The photometric redshifts in the top left/right panel are computed without using the deep u^*/z' band respectively. The bottom left panel shows the photometric redshifts for a NIR selected sample. The bottom right panel shows the photometric redshifts obtained using the B, V, R, I bands from the VVDS survey.

4 fields. However, we observe significant variations of the redshift distribution between the 4 fields. Fig.17 shows the ratio between the redshift distribution in each field and the redshift distribution averaged over the 4 fields, using a redshift step of $\Delta z = 0.1$. This ratio shows that the variations between two fields can reach a factor 2. The average dispersion over the redshift range [0.2-1.5] is $\sim$ 20%. and deacreases with the redshift since the comoving volumed surveyed increases with the redshift. We conclude that the cosmic variance already affects fields larger than 0.7 deg^2.

8. Conclusions

Using the unprecedented combination of the deep $u^*g'r'i'z'$ multi-band imaging data from the CFHTLS-D1, shallower $BVRI$ data from the VVDS imaging survey (supplemented by J and K data on a limited subsample) and VVDS first epoch spectroscopic redshifts, we have been able to obtain very accurate photometric redshifts on the CFHTLS-D1 field. We reach $\sigma_{\Delta z/(1+z)} = 0.037$

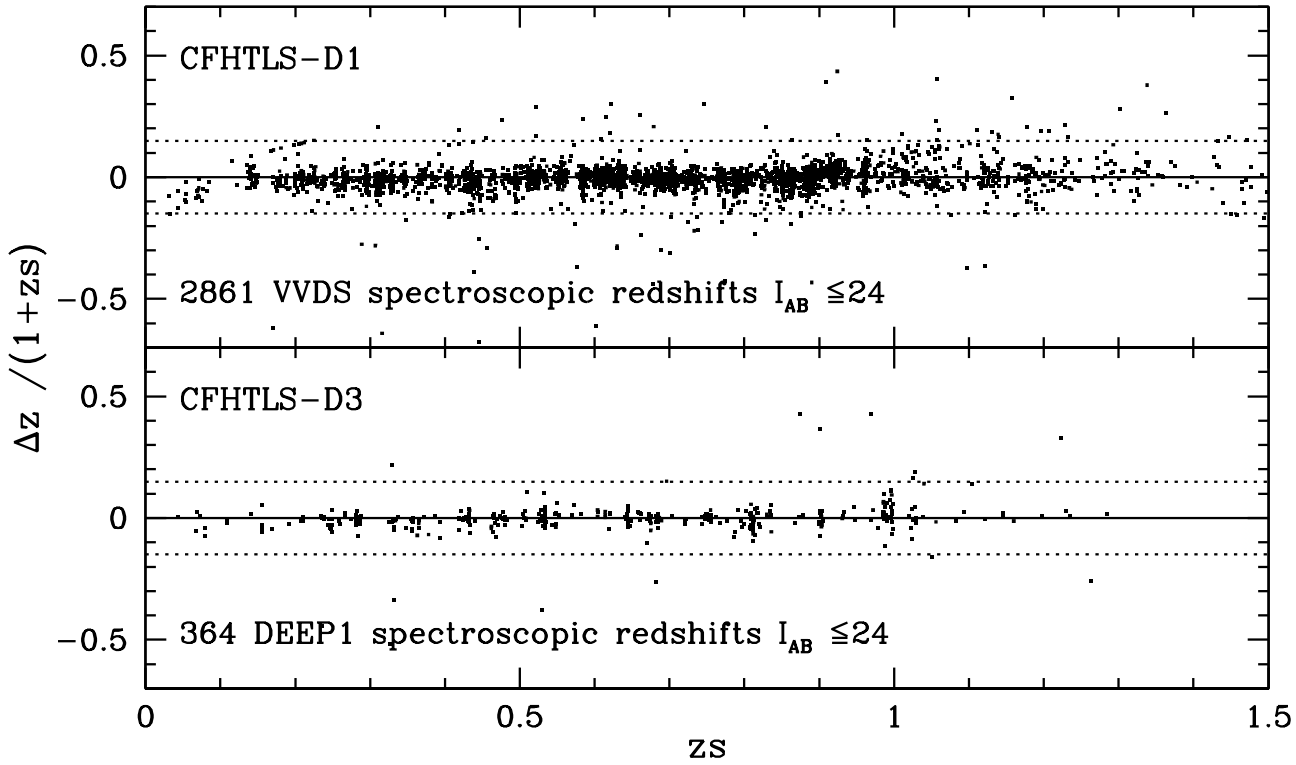

Fig. 14. Δz as a function of redshift. The photometric redshifts are computed using the CFHTLS filter set u^*, g', r', i', z'. The top panel and bottom panels present the photometric redshifts obtained on the CFHTLS-D1 and CFHTLS-D3 fields respectively.

at $i' \leq 24$ and $\eta = 3.7\%$ of catastrophic errors (defined strictly as $\Delta z > 0.15(1+z)$). For the bright selected sample $i_{AB} \leq 22.5$, we reach $\sigma_{\Delta z/(1+z)} = 0.030$ and $\eta = 1.7\%$.

This accuracy is obtained thanks to the calibration of photometric redshifts on a large and deep spectroscopic sample of 2867 galaxies. We have established a reliable calibration method combining an iterative correction of photometric zero-points, template optimization, and a Bayesian approach. This method removes some clear systematic trends in the estimate and reduces by a factor 2.3 the fraction of catastrophic errors.

We have investigated in detail the quality of photometric redshifts as a function of type, apparent magnitude and redshift based on the comparison with the VVDS spectroscopic redshifts. This step is crucial for forthcoming scientific analysis. As expected we find that the apparent magnitude is the key parameter: the fraction of catastrophic errors increases by a factor 12 and the rms by a factor 1.7 between $17.5 \leq i'_{AB} \leq 21.5$ and $23.5 \leq i'_{AB} \leq 24$. The reliability of the photometric redshifts also depends on the spectral type: half of the catastrophic errors are associated to starburst galaxies. The evolution of η as a function of redshift shows that the redshift range the most appropriate for forthcoming scientific analysis is $0.2 < zp < 1.5$. This range can be extended in the 'redshift desert' when NIR data are available (only 6% of the field is covered so far).

We present i' band selected redshift distributions at $i'_{AB} \leq 23$ and $i'_{AB} \leq 24$, fully compatible with the N(z) measured from the VVDS spectroscopic redshift. We show the ability of the technique to correctly recover the redshift distributions, even identifying the strongest density peaks. We show that a NIR selected sample is very efficient to target high redshift galaxies, with 40% of the sample at $z > 1$ for $K \leq 23$. This robust K selected sample will be used to investigate the evolution of the stellar mass function (Pozzetti et al. 2006, in preparation) which is a crucial test on the hierarchical model (e.g. Kauffmann & Charlot 1998, Cimatti et al. 2002, Somerville et al. 2004).

Finally, we have applied our robust photometric redshifts measurements code on the four CFHTLS deep fields (*http://www.cfht.hawaii.edu/Science/CFHTLS*). We measure photometric redshifts for an unprecedented large and deep sample of 522286 objects at $i'_{AB} \leq 25$ on 3.11 deg^2. We assess the accuracy of these photometric redshifts beyond the spectroscopic limits and we present the redshift distributions in these four deep fields showing that cosmic variance effect is present on fields of 0.7-1 deg^2.

We release the photometric redshifts described in this paper to the Canadian and France communities at *http//....*

Acknowledgements. Based on observations obtained with MegaPrime/MegaCam, a joint project of CFHT and CEA/DAPNIA, at the Canada-France-Hawaii Telescope (CFHT) which is operated by the National Research Council (NRC) of Canada, the Institut National des Sciences de l'Univers of the Centre National de la Recherche Scientifique (CNRS) of France, and the University of Hawaii. This work

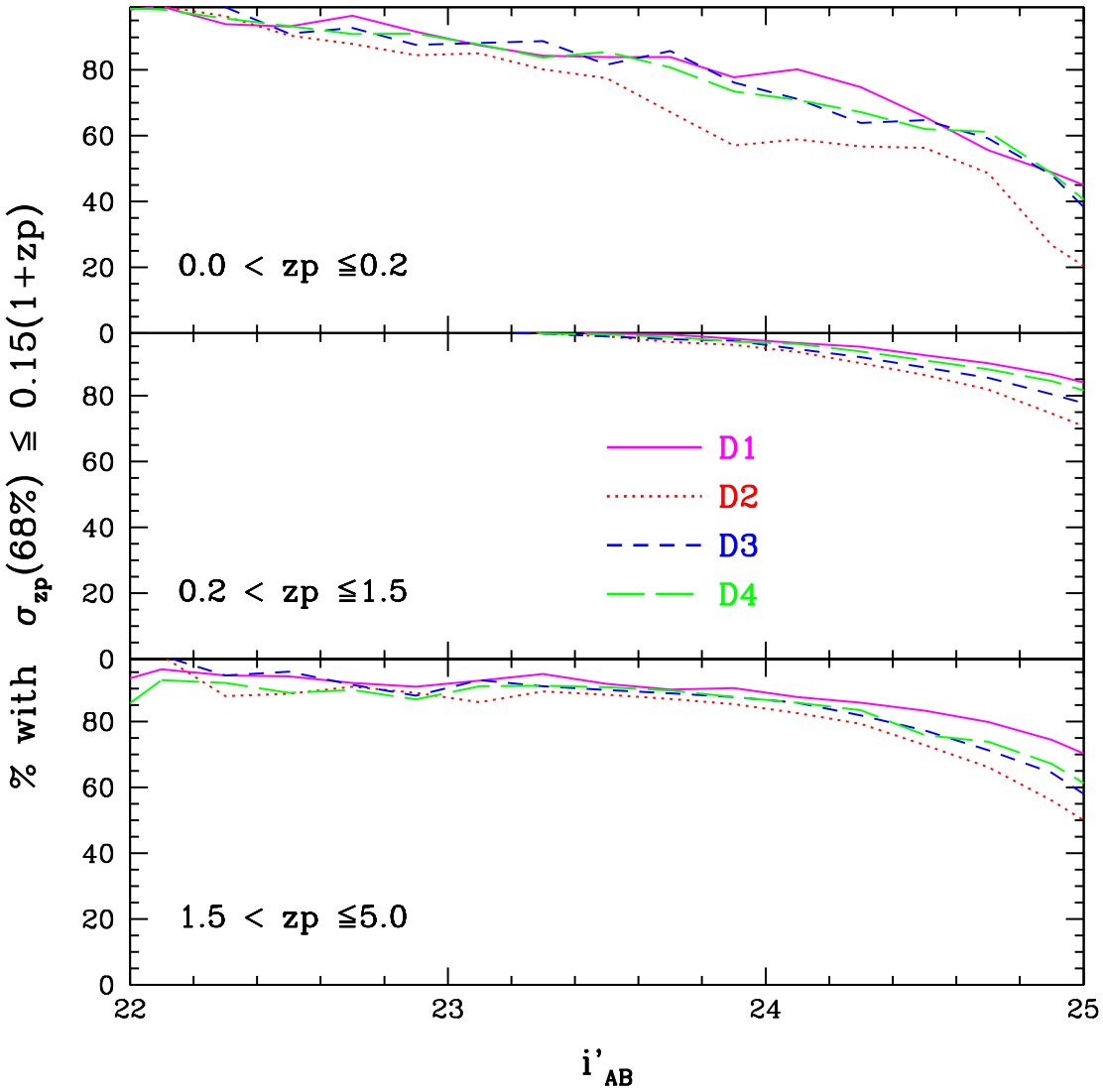

Fig. 15. Fraction of photometric redshifts with an error bar at 68% larger than $0.15 \times (1 + zp)$, as a function of i' apparent magnitude. This statistic is shown in the 4 CFHTLS deep fields D1 (solid line), D2 (dotted line), D3 (short dashed line) and D3 (long dashed line) and in the three redshift ranges $0 < z \leq 0.2$ (top panel), $0.2 < z \leq 1.5$ (middle panel) and $1.5 < z \leq 5$ (bottom panel).

is based in part on data products produced at TERAPIX and the Canadian Astronomy Data Centre as part of the Canada-France-Hawaii Telescope Legacy Survey, a collaborative project of NRC and CNRS. This research has been developed within the framework of the VVDS consortium. We thank the ESO staff at Paranal for their help in the acquisition of the data. This work has been partially supported by the CNRS-INSU and its Programme National de Cosmologie (France) and Programme National Galaxies (France), and by Italian Ministry (MIUR) grants COFIN2000 (MM02037133) and COFIN2003 (num.2003020150). The VLT-VIMOS observations have been carried out on guaranteed time (GTO) allocated by the European Southern Observatory (ESO) to the VIRMOS consortium, under a contractual agreement between the Centre National de la Recherche Scientifique of France, heading a consortium of French and Italian institutes, and ESO, to design, manufacture and test the VIMOS instrument.

References

Arnouts S., Cristiani S., Moscardini L. et al., 1999, MNRAS, 310, 540
Arnouts S., Moscardini L., Vanzella E. et al., 2002, MNRAS, 329, 355
Baum W. A., 1962, IAU Symp., 15, 390
Benítez N., 2000, ApJ, 536, 571
Benítez N., Ford H., Bouwens R. et al., 2004, ApJS, 150, 1
Bertin E. & Arnouts S., 1996, A&AS, 117, 393
Bolzonella M., Miralles J.-M. & Pelló R., 2000, A&A, 363, 476
Bolzonella M., Pelló R., & Maccagni D., 2002, A&A, 395, 443
Brodwin M., Lilly S.J., Porciani C. et al., 2006, ApJS, 162, 20
Bruzual G. et Charlot S., 2003, MNRAS, 344, 1000
Budavári T., Szalay A. S., Connolly A. J., Csabai I. & Dickinson M., 2000, AJ, 120, 1588
Coleman G.D., Wu C.-C., Weedman D.W., 1980, ApJS, 43, 393

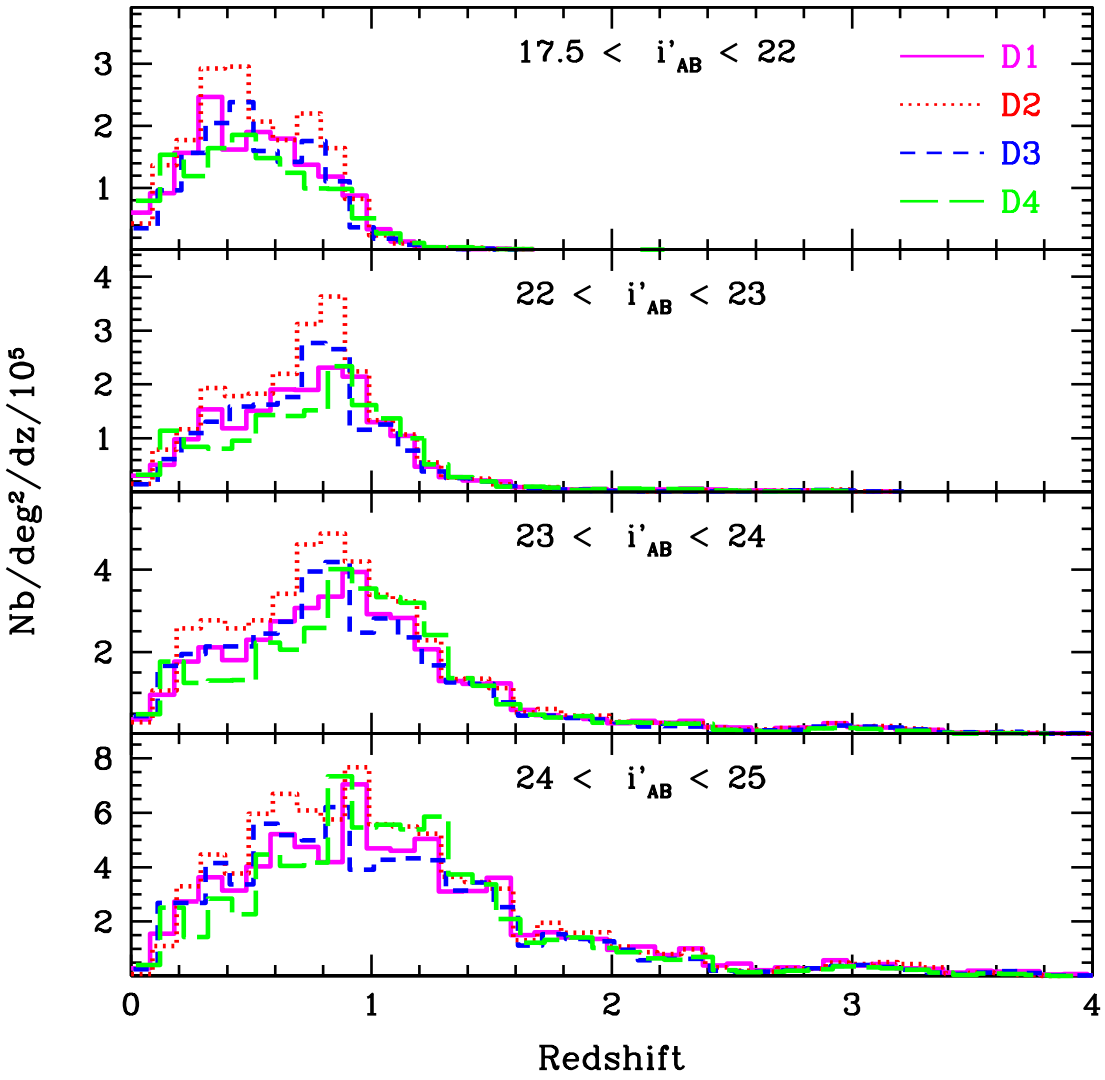

Fig. 16. Photometric redshift distributions in the 4 fields CFHTLS-D1 (solid line), CFHTLS-D2 (dotted line), CFHTLS-D3 (short dashed line) and CFHTLS-D4 (long dashed line). The redshift distribution are shown from bright ($17.5 < i'_{AB} < 22$) to faint selected samples ($24 < i'_{AB} < 25$) from the top to the bottom, respectively.

Connolly A. J., Csabai I., Szalay A. S., Koo D. C., Kron R. G., & Munn J. A., 1995, AJ, 110, 2655

Csabai I., Connolly A. J., Szalay A. S. & Budavári T., 2000, AJ, 119, 69

Cimatti A., Pozzetti L., Mignoli M. et al., 2002, A&A, 391, L1

Fernández-Soto A., Lanzetta K. M. & Yahil A., 1999, ApJ, 513, 34

Fioc M. & Rocca-Volmerange B., 1997, A&A, 326, 950

Fontana A., D'Odorico S., Poli F. et al., 2000, AJ, 120, 2206

Gabasch A., Bender R., Seitzer S. al., 2004, A&A, 421, 41

Ilbert O., Tresse L., Zucca E. et al., 2005, A&A, 439, 863

Iovino A., McCracken H.J., Garilli B. et al., 2005, A&A, in press, astro-ph/0507668

James F. & Roos M., 1995, MINUIT Function Minimization and Error Analysis, Version 95.03, CERN Program Library D506

Kauffmann G. & Charlot S., 1998, MNRAS, 297, L23

Kinney A.L., Calzetti D., Bohlin R.C., McQuade K., Storchi-Bergmann T. & Schmitt H.R., 1996, ApJ, 467, 38

Kron R.G., 1980, ApJS, 43, 305

Le Fèvre O., Mellier Y., McCracken H. J. et al., 2004a, A&A, 417, 839

Le Fèvre O., Vettolani G., Paltani S. et al., 2004b, A&A, 428, 1043

Le Fèvre O., Vettolani G., Garilli B. et al., 2005a, A&A, 439, 845

Le Fèvre O., Paltani P., Arnouts S. et al., 2005b, nature, submitted

Madau P., 1995, ApJ, 441, 18

McCracken H.J., Radovich M., Bertin E. et al., 2003, A&A, 410, 17

McCracken H. J. et al., 2006, A&A, in preparation

Mobasher B., Idzi R., Bentez N. et al., 2004, ApJL, 600, L167

Pickles A. J., 1998, PASP, 110, 863

Phillips A.C., Andrew C., Guzman R. et al., 1997, ApJ, 489, 543

Pozzetti L. et al., 2006, A&A, in preparation

Prevot M.L., Lequeux J., Prevot L., Maurice E. & Rocca-Volmerange B., 1984, A&A, 132, 389

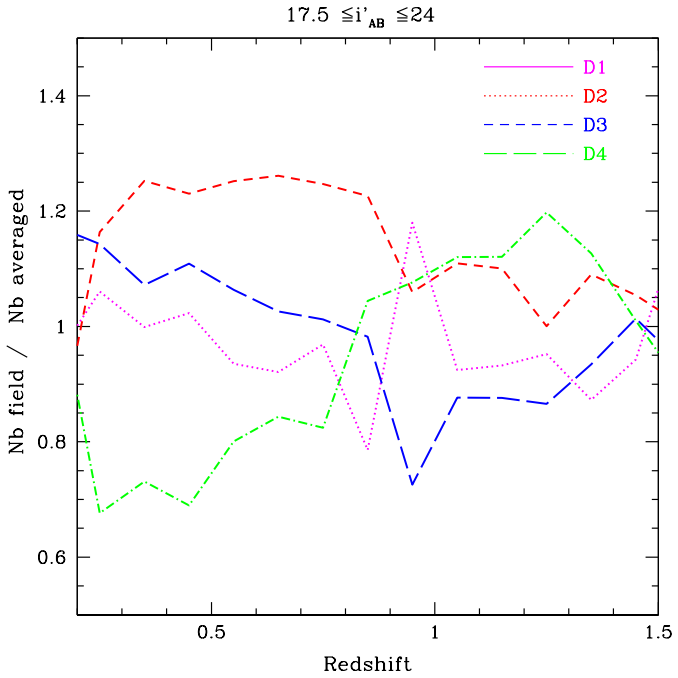

Fig. 17. Ratio between the redshift distributions in each field and the redshift distribution averaged over the 4 fields. Symbols for each field are the same than Fig.16.

Puschell J.J., Owen F.N. & Laing R.A., 1982, ApJL, 257, L57
Sawicki M.J., Lin H. & Yee H.K.C., 1997, AJ, 113, 1
Schlegel D. J., Finkbeiner D. P., & Davis M., 1998, ApJ, 500, 525
Somerville R.S., Moustakas L.A., Mobasher B. et al., 2004, ApJL, 600, L135
Vanzella E., Cristiani S., Fontana A. et al., 2004, A&A, 423, 761
Wang Y., Bahcall N. & Turner E.L., 1998, AJ, 116, 2081
Wolf C., Meisenheimer K., Rix H.-W. et al., 2003, A&A, 401, 73
Wolf C., Meisenheimer K., Kleinheinrich M. et al., 2004, A&A, 421, 913